Long-term litter decomposition controlled by manganese redox cycling

Citation	Keiluweit, M., Nico, P., Harmon, M. E., Mao, J., Pett-Ridge, J., & Kleber, M. (2015). Long-term litter decomposition controlled by manganese redox cycling. Proceedings of the National Academy of Sciences, 112(38), E5253-E5260. doi:10.1073/pnas.1508945112
DOI	10.1073/pnas.1508945112
Publisher	National Academy of Sciences
Version	Version of Record
Terms of Use	http://cdss.library.oregonstate.edu/sa-termsofuse

Long-term litter decomposition controlled by manganese redox cycling

Marco Keiluweit[a,b,1,2], Peter Nico[c], Mark E. Harmon[d], Jingdong Mao[e], Jennifer Pett-Ridge[b], and Markus Kleber[a,f]

[a]Soils Division, Department of Crop and Soil Science, Oregon State University, Corvallis, OR 97330; [b]Chemical Sciences Division, Lawrence Livermore National Laboratory, Livermore, CA 94550; [c]Earth Sciences Division, Lawrence Berkeley National Laboratory, Berkeley, CA 94720; [d]Department of Forest Ecosystems and Society, Oregon State University, Corvallis, OR 97331; [e]Department of Chemistry and Biochemistry, Old Dominion University, Norfolk, VA 23529; and [f]Institut für Bodenlandschaftsforschung, Leibnitz-Zentrum für Agrarlandschaftsforschung (ZALF), 15374 Muuncheberg, Germany

Edited by François M. M. Morel, Princeton University, Princeton, NJ, and approved August 18, 2015 (received for review May 8, 2015)

Litter decomposition is a keystone ecosystem process impacting nutrient cycling and productivity, soil properties, and the terrestrial carbon (C) balance, but the factors regulating decomposition rate are still poorly understood. Traditional models assume that the rate is controlled by litter quality, relying on parameters such as lignin content as predictors. However, a strong correlation has been observed between the manganese (Mn) content of litter and decomposition rates across a variety of forest ecosystems. Here, we show that long-term litter decomposition in forest ecosystems is tightly coupled to Mn redox cycling. Over 7 years of litter decomposition, microbial transformation of litter was paralleled by variations in Mn oxidation state and concentration. A detailed chemical imaging analysis of the litter revealed that fungi recruit and redistribute unreactive Mn^{2+} provided by fresh plant litter to produce oxidative Mn^{3+} species at sites of active decay, with Mn eventually accumulating as insoluble $Mn^{3+/4+}$ oxides. Formation of reactive Mn^{3+} species coincided with the generation of aromatic oxidation products, providing direct proof of the previously posited role of Mn^{3+}-based oxidizers in the breakdown of litter. Our results suggest that the litter-decomposing machinery at our coniferous forest site depends on the ability of plants and microbes to supply, accumulate, and regenerate short-lived Mn^{3+} species in the litter layer. This observation indicates that biogeochemical constraints on bioavailability, mobility, and reactivity of Mn in the plant–soil system may have a profound impact on litter decomposition rates.

terrestrial carbon cycle | nutrient cycling | forest soil ecosystems | soil-atmosphere interactions | climate change

Decomposition of above-ground plant detritus (litter) is a fundamental process regulating the release of nutrients for plant growth and the formation of soil organic matter (SOM) in forest ecosystems (1). Litter decomposition regulates the proportion of litter-derived carbon (C) that is either retained in the system as SOM or lost as CO_2 (2), thereby influencing net C storage in soils. Although even small decomposition rate increases may accelerate climate change by virtue of increasing CO_2 emissions from soils (3), uncertainty persists over the rate-controlling mechanisms (4, 5).

Litter decomposition rates are strongly influenced by climatic factors (e.g., temperature and moisture) and have long been linked to litter chemistry, specifically lignin content (6). Lignin—an aromatic biopolymer—often makes up between 15% and 40% of the litter mass and is concentrated in cell walls (7). It encrusts cellulose microfibrils to form protective physical units ("ligno–cellulose complexes") that are embedded in a matrix of hemicellulose. Conventional thinking suggests that the relatively high initial litter decomposition rates are due to the preferential use of soluble and readily accessible polysaccharides and hemicelluloses relative to lignin components. In later stages, decomposition slows when litter has become enriched in lignin and any remaining celluloses and hemicelluloses remain enclosed and protected in ligno–cellulose complexes (8). However, more recent research suggests that lignin readily decomposes in the presence of dissolved organic substrates (5). This effect was attributed to dissolved and readily assimilable substrates providing decomposer organisms with the extra energy required for the cometabolic breakdown of lignin. This observation suggests that litter decomposition may be controlled not only by litter chemistry, but also by the availability of key resources for the efficient microbial breakdown of individual biopolymers.

One such key resource seems to be manganese (Mn). Numerous studies (9–14) have measured a strong positive relationship between Mn content of litter and litter decomposition (expressed as % mass loss) in boreal, temperate, and semiarid forest ecosystems. Among all other parameters tested (water soluble C, lignin, N, P, K, Ca, and Mg contents), Mn content best predicted litter mass loss, leading Berg et al. (10) to conclude that "Mn concentration is the single main factor" governing litter decomposition in these forest biomes. However, efforts to experimentally validate the effect of Mn availability on decomposition rates have produced ambiguous results (15) and have been hampered by the lack of explicit consideration of Mn redox cycling in the soil system.

Microbial Mn oxidation has long been implicated in the enzymatic degradation of lignin (16). Culture studies with lignin-decomposing fungi showed that trivalent Mn^{3+} is generated during the oxidation of lignin model compounds (17). It has been proposed that Mn^{3+} is formed via the oxidation of soluble Mn^{2+} by fungal exo-enzymes, such as Mn peroxidase or phenol oxidases (e.g., laccase). When stabilized in solution by chelating ligands, these soluble Mn^{3+}–ligand complexes were suggested to act as diffusible and potent oxidants of lignin analogs (16). More recently, it was discovered not only that fungi can oxidize Mn enzymatically, but that a diverse range of heterotrophic bacteria

Significance

The rate-controlling mechanisms of litter decomposition are of fundamental importance for ecosystem nutrient cycling, productivity, and net carbon (C) balance. Current C cycling models rely primarily on climatic factors and lignin content as the main predictors of litter decomposition rates. Here, we show how the ability of the integrated plant–soil system to promote active redox cycling of manganese (Mn) regulates litter decomposition. Our work suggests that incorporating the coupling of litter decomposition and other elemental cycles, such as the Mn cycle, into conceptual and numerical models may significantly improve our mechanistic understanding and predictions of C cycling in terrestrial ecosystems.

Author contributions: M. Keiluweit, P.N., M.E.H., J.P.-R., and M. Kleber designed research; M. Keiluweit performed research; J.M. contributed new reagents/analytic tools; M. Keiluweit analyzed data; and M. Keiluweit, P.N., J.P.-R., and M. Kleber wrote the paper.

The authors declare no conflict of interest.

This article is a PNAS Direct Submission.

[1]Present address: Stockbridge School of Agriculture, University of Massachusetts, Amherst, MA 01003.

[2]To whom correspondence should be addressed. Email: keiluweit@umass.edu.

This article contains supporting information online at www.pnas.org/lookup/suppl/doi:10.1073/pnas.1508945112/-/DCSupplemental.

isolated from terrestrial and aquatic systems can do so as well (18, 19). Despite the widespread physiological potential for microbial Mn oxidation, it is unclear to what extent the natural Mn redox cycle is coupled to organic matter degradation in forest ecosystems.

Circumstantial evidence suggests that microbial oxidation may be the main driver of Mn cycling in forest litter layers. Foliar litter is a major source of Mn compared with other plant litter and mineral soils (20). Mn in live foliage is naturally present in its reduced, mobile form (i.e., Mn^{2+}), facilitating its supply to photosystem II and other enzymatic systems (21). Foliar litter becomes enriched in Mn relative to fresh plant material and further accumulates Mn during the decomposition process (9, 22). Mn in dead foliage (i.e., litter) was found to be bound in organic complexes (23), but it is unclear whether Mn is present as unreactive Mn^{2+} or the more reactive Mn^{3+} form. A recent spectroscopic investigation showed that foliar tissue contains predominantly Mn^{2+} that is gradually oxidized to $Mn^{3+/4+}$-oxides in the soil upon decomposition (24). This observation led Herndon et al. (24) to suggest that Mn stored in leaves is solubilized upon litter fall but rapidly immobilized as $Mn^{3+/4+}$ oxides after aging in the soil. Others have observed Mn-rich black precipitates on needle litter colonized by fungi (25), resembling $Mn^{3+/4+}$ oxides as observed after fungal Mn oxidation in model systems (26, 27).

Here, we investigated the impact of biotic Mn redox cycling on long-term litter decomposition in forest ecosystems, taking advantage of a field experiment conducted in an old-growth Douglas-fir forest in the Oregon Cascades. During this 7-y experiment, each year's litterfall was spatially separated by nylon mesh placed on the forest floor. The mesh created a series of six well-confined litter layers (a "littercake") containing Douglas-fir needles at increasing decomposition stage. Our approach was to resolve Mn transformation and litter decomposition within the forest ecosystem at two different scales—across the whole soil profile and in microenvironments on needles colonized by fungi. Across the litter layer, we hypothesized that Mn oxidation covaries with the breakdown of aromatic litter components (i.e., lignins and tannins). Changes in Mn chemistry were identified by selective extractions and X-ray absorption near edge structure (XANES) spectroscopy, whereas the alterations in the molecular composition of litter was determined using a combination of Fourier-transform infrared (FTIR) spectroscopy, NMR, and laser desorption postionization mass spectrometry (LDPI-MS). Within microenvironments on needle surfaces, we anticipated that oxidative degradation of aromatic compounds occurs where fungi produce Mn^{3+}. To spatially resolve Mn oxidation state and chemical transformations in these microenvironments, we applied a multimodal chemical imaging approach that coupled microscale X-ray fluorescence (μXRF)/X-ray absorption spectroscopy (XAS) with μFTIR imaging.

Results

Mn Transformations. With increasing litter age, Mn gradually accumulated and became more oxidized. Total Mn concentrations in decomposing needle litter progressively increased and, on dry-weight basis, became higher than in fresh needles or the underlying mineral horizons (Table S1). The contribution of pyrophosphate-extractable Mn (Mn_{PYRO}, Mn in soluble and organically complexed pools) increases most rapidly in the first three layers, before reaching a plateau in layer 4 (Table S1).

Concurrently, Mn XANES absorption maxima shifted from energies associated with Mn^{2+}-dominated phases to Mn^{3+}- and Mn^{4+}-rich phases as litter age increased (Fig. 1). The average oxidation state of Mn calculated from these shifts progressively increased from +2.07 in fresh needles to +2.74 in layer 6 (Fig. 1). The relative amount of Mn^{3+} species increased most rapidly in layers 1 and 2 whereas that of Mn^{4+} species increased strongly from layers 3–6. Needles in the underlying O horizons showed another slight increase in average oxidation state (+2.83). Mn oxidation state (+3.1 and +3.0) and, consequently, the relative contributions of Mn^{3+} and Mn^{4+} were found to be highest in the mineral soil.

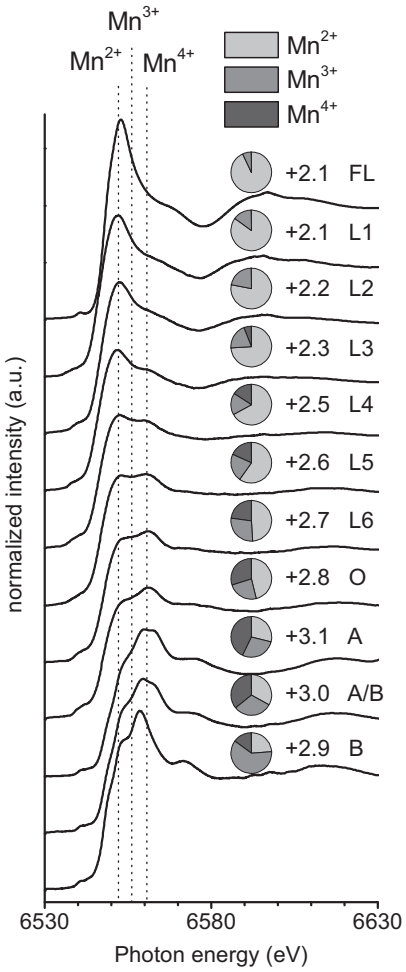

Fig. 1. Change in Mn speciation in Douglas-fir needle litter (L) over 6 years of decomposition. Mn K-edge XANES spectra with approximate positions of absorption maxima for Mn^{2+}, Mn^{3+}, and Mn^{4+} forms (50). Pie chart *Insets* show the relative amounts of Mn^{2+}, Mn^{3+}, and Mn^{4+} with the adjacent number representing the average oxidation state as determined by linear combination fitting (50). Fresh needle litter (FL) and the underlying organic (O) and mineral (A and B) horizons were included for comparison.

Litter Decomposition. Overall, we observed a strong relationship between Mn redox transformations and litter decomposition. The increase of Mn in soluble and organically complexed pools (Mn_{PYRO}) was significantly correlated with microbial processing of the litter. The C/N ratio, which might be expected to decrease with increased microbial processing, decreased most rapidly from layers 1–3 (Table S1). This decrease in C/N was correlated with increases in Mn_{PYRO} ($R^2 = 0.76$, $P < 0.05$) (see Fig. 3*A*), but not with changes in organically complexed Al, Ca, or Fe ($P > 0.05$). Similarly, the FTIR absorbance of amide groups, associated with microbial protein and chitin, increased (Fig. 2*A*) and is positively correlated with Mn_{PYRO} ($R^2 = 0.94$, $P < 0.05$) (Fig. 3*B*).

Differences in the litter's molecular composition correspond with increases in Mn oxidation state across the decomposition sequence. FTIR spectra show that the relative absorbance of regions associated with saccharide and aromatic functional groups (Fig. 2*A*) is significantly correlated with Mn oxidation

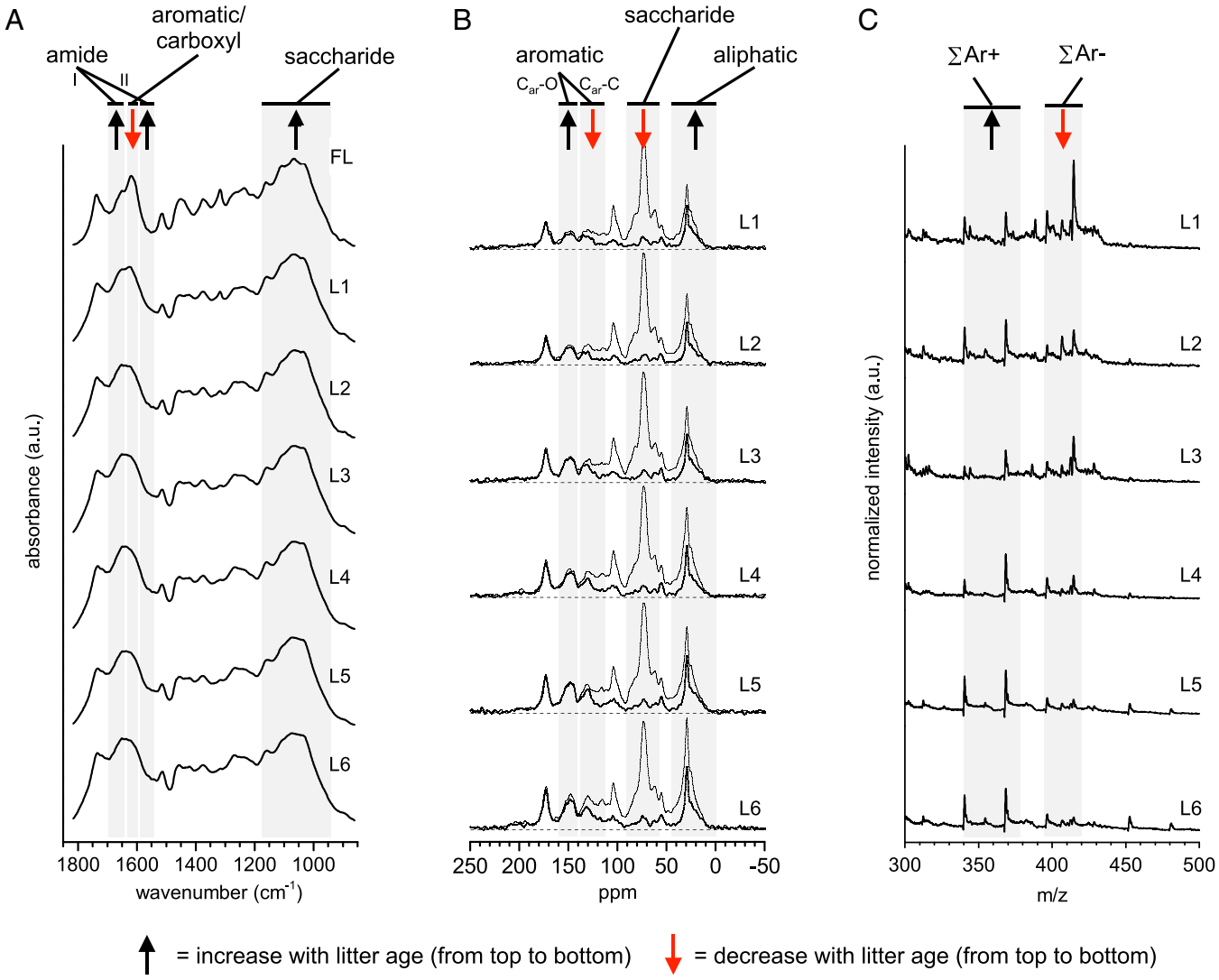

Fig. 2. Chemical transformations of Douglas-fir needles over 6 y of decomposition. (*A*) FTIR spectra of needle litter. Absorbance of both (*i*) amide I and II groups associated with bacterial/fungal protein and chitin increased and (*ii*) C-O-C groups of polysaccharides increased with litter age whereas (*iii*) absorbance of COO-stretch of carboxylates and the ar-C-C stretch of aromatic lignin decreased. (*B*) ^{13}C-NMR spectra of needle litter. Gray lines show spectra obtained by unselective CP/TOSS experiments including all carbons, whereas black lines show spectra obtained by selective CP/TOSS-DD sensitive to nonprotonated carbons and mobile carbons (e.g., -CH_3 and long-chain -$(CH_2)_n$-). (*C*) Synchrotron-LDPI mass spectra of needle litter. Fragments with *m/z* of 340, 370, 396, 399, 400, 406, and 414 showed ionization energies of ≤8.5 eV and were thus assigned to aromatic structures. Detailed description of peak assignments can be found in *SI Materials and Methods*. $\sum ar^+$ denotes the sum of normalized intensities of peaks that increase with litter age (*m/z* = 340 and 370) whereas $\sum ar^-$ represents the sum of normalized intensities of peaks decreasing over time (*m/z* = 396, 399, 400, 406, and 414). Mass spectra presented here were collected with a photon energy of 9.5 eV and were chosen because they showed less fragmentation and greater signal-to-noise ratio.

state (R^2 = 0.79, P < 0.05) (Fig. 3*C*). Similarly, relative changes in the abundance of saccharide and aromatic moieties in the ^{13}C NMR spectra (Fig. 2*B*) are well correlated with Mn oxidation (R^2 = 0.98, P < 0.05) (Fig. 3*D*).

To evaluate a link between the chemical alteration of aromatic litter components and Mn transformations, we gathered ^{13}C NMR and synchrotron-LDPI mass spectrometry data. Two different types of aromatic carbons are usually identified in ^{13}C NMR spectra: protonated (C_{ar}-H) and quaternary nonoxygenated (C_{ar}-C) at 142–110 ppm, or oxygenated aromatic ring carbons (C_{Ar}-O) at 162–142 ppm (28). The abundance of oxygenated relative to nonoxygenated aromatic ring carbons (C_{ar}-O/C_{ar}-R, with R = C or H) in ^{13}C NMR spectra, used here as a proxy for ring oxidation, was strongly correlated with changes in Mn_{PYRO} (R^2 = 0.92, P < 0.05) (Fig. 3*E*). Synchrotron-LDPI is a soft-ionization mass spectrometry technique that is particularly sensitive for lignin-derived compounds (29, 30). Inspection of the resulting mass spectra showed that one set of peaks at lower mass-to-charge (*m/z*) ratios ($\sum ar^+$; *m/z* = 340–370) gains intensity with increasing litter age whereas the intensity of a second set of peaks at higher *m/z* ratios ($\sum ar^-$, *m/z* = 396–414) declines (Fig. 2*C*). To confirm that these mass fragments (i.e., *m/z* = 340, 370, 396, 399, 400, 406, and 414) correspond to aromatic structures, we determined ionization energies (IEs) for each of the fragments in a second LDPI experiment as previously described (31, 32) and detailed in *SI Materials and Methods*. This method exploits the fact that aromatic ring structures have lower ionization energies (≤8.5 eV) than other organic moieties (>9 eV) (29, 30). Because ionization energies of these mass fragments ranged from 7.3 to 8.5 eV (Table S2), we attributed these peaks to aromatic moieties. The observed gradual transition from one set of aromatic compounds to the other ($\sum ar^+/\sum ar^-$) therefore points to a structural

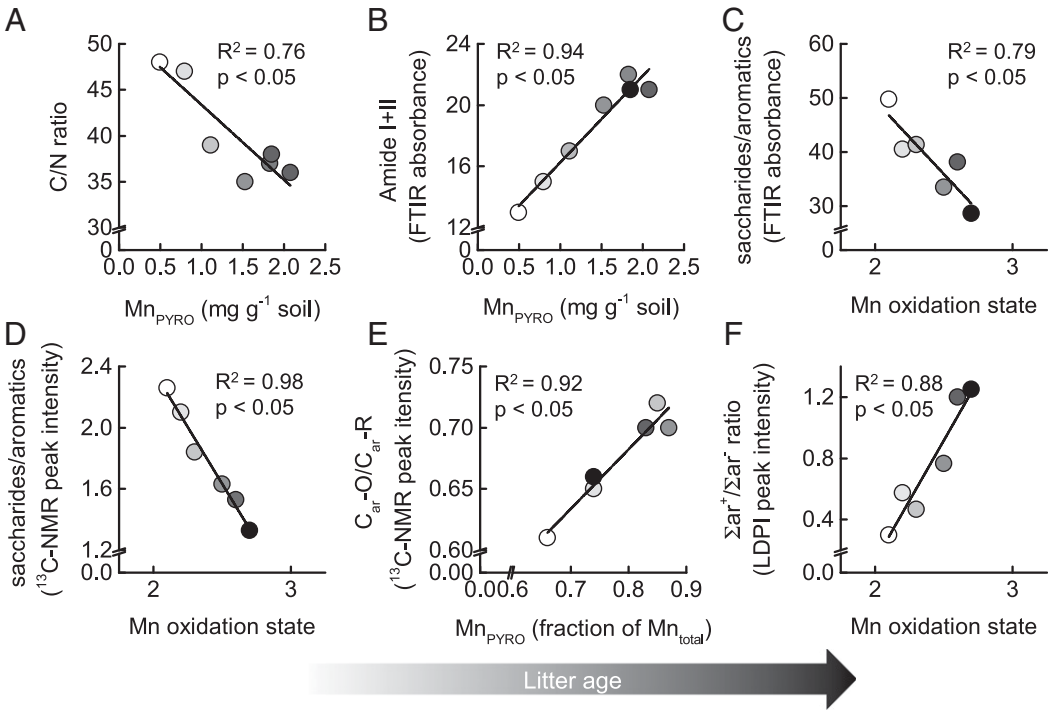

Fig. 3. Covariation of litter and Mn transformations in Douglas-fir needles over 6 y of decomposition. (*A*) Changes in the C/N ratio across the litter layer in relation to pyrophosphate-extractable Mn (Mn_{PYRO}), here used as a proxy for bioavailable Mn. (*B*) Changes in the FTIR absorbance of amide I and II groups as a proxy for microbial protein/chitin abundance relative to variations in average Mn oxidation state. (*C*) Changes in litter decomposition (expressed by the ratio of saccharide/aromatic carbon absorbance in the FTIR spectra) in relation to Mn oxidation state. (*D*) Changes in litter decomposition (as indicated by the ratio of saccharide/aromatic carbon in ^{13}C NMR spectra) in relation to Mn oxidation state. (*E*) Lignin transformations (expressed by the ratio of C_{ar}-O/C_{ar}-C in the ^{13}C NMR spectra) in relation to average Mn oxidation state. (*F*) Changes in lignin transformations (expressed by the relative ratio in signal intensity of LDPI-detected aromatic mass fragments shown in Fig. 2*C*) in relation to average Mn oxidation state.

change in aromatic litter components, which showed a strong correlation with Mn oxidation state (Fig. 3*F*) ($R^2 = 0.88$, $P < 0.05$).

Mn Form and Distribution on Decomposing Needle Surfaces. Because Mn chemistry and molecular composition of the litter changed more rapidly in the initial stages of decomposition, we chose needles from layer 1 for detailed imaging analysis. These needles were colonized by fungi forming dense hyphal networks with distinct dark patches hypothesized to be $Mn^{3+/4+}$ oxides (Fig. S1*A*). Elemental maps of resin-embedded cross-sections from three needles showed that Mn concentrated in diffuse patches on the surface, associated either with individual hyphae or larger particles (Fig. S1*B*). Other major elements (e.g., Ca, Fe, and Si) were randomly distributed. Mn XANES spectra collected from diffuse patches and discrete particles on the needle surface showed a greater abundance of Mn^{3+} and Mn^{4+} and, consequently, a higher average oxidation state than those extracted from individual hyphae and the needle tissue (Fig. S1*C*).

Manganese Chemistry at the Hyphae–Epidermis Interface. Photographs of two cryo-sectioned decomposing needles show dark hyphae colonizing the epidermis region (Fig. 4*A*). Along this interface, μFTIR chemical imaging visually separates needle tissue rich in aromatic structures from amide-rich fungal materials (Fig. 4*B*). Elemental maps of this interface showed that Mn accumulates where fungal hyphae are in direct contact with the needle epidermis (Fig. 4*C*). We collected Mn XANES spectra from hotspots (points 3–5, Fig. 4*C*) along this interface (Fig. 4*D*). Spectral deconvolution indicated that the hotspots associated with fungi on the needle surface were more oxidized (points 3–5; average oxidation state, 2.6–2.7) than Mn in the needle interior (points 1–2; average oxidation state, 2.1–2.2) (Fig. 4*C*). Interestingly, these hotspots of oxidized Mn were colocalized with carbonyl groups (1,750-1,680 cm^{-1}) as shown in the μFTIR absorbance map (Fig. 4*B*).

To further investigate the potential chemical alterations due to oxidative Mn species at the site of direct contact between fungal hyphae and the needle surface, we extracted μFTIR spectra along a transect across this interface (red line, Fig. 4*B*). Spectra taken from fungal tissue, the fungi–epidermis interface (contact zone), the needle epidermis, and mesophyll are presented in Fig. 4*E*. The spectrum extracted from the infected epidermis (C) showed a lower absorbance of saccharide bands (1,180–950 cm^{-1}), as well as enhanced absorbance of bands corresponding to carbonyl (~1,700 cm^{-1}) and aromatic C = C groups (~1,600 cm^{-1}) compared with uninfected epidermis regions (Fig. 4*E*).

Discussion

We initially hypothesized that litter-decomposing fungi repurpose Mn^{2+} naturally present in litter to produce reactive Mn^{3+} species at the site of oxidative needle degradation. Our results suggest a strong relationship between biotic Mn oxidation and litter decomposition both at macroscales (litter layer) and microscales (fungal needle colonization), the causality of which is discussed in the following.

Across the Douglas-fir litter layer examined here, Mn was progressively transformed. Total Mn increased rapidly in years 1–3, followed by a slower increase in years 4–6, a trend consistent with Mn accumulation in litter layers observed elsewhere (9, 22). Similarly, the amount of pyrophosphate-extractable Mn (Mn_{PYRO}) and the proportion of Mn^{3+} as evidenced by XANES increased most rapidly within the first 3 y whereas solid Mn^{4+} phases did not occur until years 4–6 (Table S1 and Fig. 1). Pyrophosphate is expected to complex and extract dissolved and/or organically complexed Mn

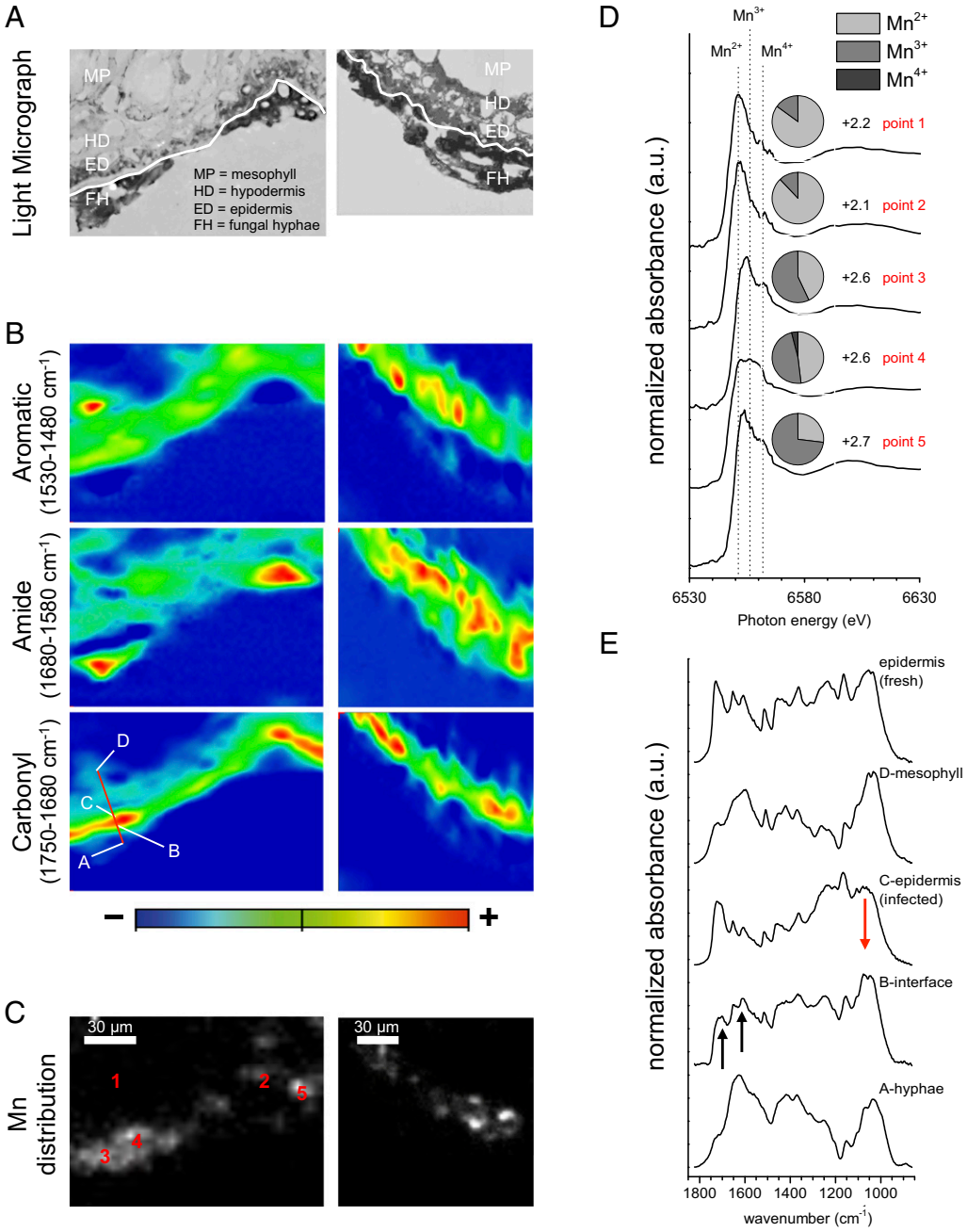

Fig. 4. Mn transformations at the hyphae–epidermis interface of two decomposing needles. (*A*) Photographs of needle thin sections showing fungal hyphae (FH) colonizing the outer walls of epidermis cells (ED), partially fungal-infected hypodermis cells (HD), and mesophyll tissue (MP). The white line delineates the boundary between fungal hyphae and the needle epidermis. (*B*) Corresponding μFTIR heat maps showing the distribution of aromatic, amide, and carbonyl functional groups. Heat maps were generated using the integrated absorbance of spectral regions given in the figure. (*C*) Corresponding Mn distribution maps of the same region of interest generated by μXRF. (*D*) Mn XANES spectra collected at locations along the hyphae–epidermis interface (points 1 and 2 in *C*) and the needle's mesophyll tissue (points 4 and 5). Pie charts show relative amounts of Mn^{2+}, Mn^{3+}, and Mn^{4+} at each location, with numbers indicating the average oxidation state. (*E*) μFTIR spectra extracted from transect across the hyphae epidermis interface, shown as red line in *B*). Note that absorbance at ~1,700 and ~1,610 cm^{-1} at the interface (B) increases relative to (C) infected epidermis regions and a fresh needle epidermis. (Scale bars: 30 μm.)

(33), which we consider a proxy for bioavailable Mn, but does not differentiate between unreactive Mn^{2+} and oxidative Mn^{3+} species. On the other hand, XANES spectroscopy can detect Mn^{3+}, without providing unambiguous information about its physical state. Combined, however, our extraction and spectroscopy results suggest the transformation of litter-borne Mn into bioavailable Mn^{2+} and reactive Mn^{3+} forms in the initial stages of decomposition. In later stages, increasing Mn oxidation resulted in $Mn^{3+/4+}$ forms similar to those observed in solid Mn oxide precipitates (24, 26, 27).

This rapid formation of bioavailable and reactive Mn forms in the first years of decomposition is accompanied by increased microbial processing of the litter. Accumulation of bioavailable and reactive Mn correlated with decreasing C/N ratios and stronger contributions of amide functionalities in the decomposing litter (Fig. 3 *A* and *B*). N content (34), fungal biomass (35), and visible fungal colonization of needle litter (36–38) commonly rise within the first 2 y of decomposition. Within a similar time frame, maxima in MnP activity can be observed (35).

Our results support the hypothesis that Mn mobilization and the formation of reactive Mn phases are caused by successive microbial colonization of the litter.

Further, the strong relationship between Mn cycling and chemical transformation of litter points to a direct involvement of Mn in the decomposition process. Mn oxidation is strongly related to the relative loss of saccharides and the transformation of aromatic litter components (Fig. 3). Oxidative transformations of aromatic compounds occurred across the litter layer, reflected in changes in abundance of aromatic compounds (Fig. 2*C*) and increases in oxygenated aromatic ring carbons (Fig. 2 *A* and *B*). These transformations were significantly correlated with Mn mobilization and oxidation (Fig. 3 *E* and *F*), suggesting that decomposing fungi actively cycle Mn for the purpose of using oxidized Mn species in the breakdown of aromatic structures.

Our imaging analysis can be reconciled as evidence that fungi actively promote Mn transport and oxidation during litter colonization. The high concentrations of Mn found in single hyphae and dense hyphal networks (Fig. S1*B*) imply biotic accumulation and transport of Mn in the litter layer. Greater contribution of Mn^{3+} and Mn^{4+} forms to overall Mn concentrations in hyphae further indicate active biotic Mn oxidation. In addition to Mn associated with fungal hyphae, we observed larger, Mn-rich particles consisting predominantly of $Mn^{3+/4+}$ forms on needle surfaces. A significant fraction of hyphae found on needle surfaces can be assumed dead (36–38), and Blanchette (25) showed dead wood-colonizing hyphae covered in Mn precipitates. These observations suggest that, when the fungal supply of Mn^{3+}-stabilizing chelators such as oxalic acid ceases upon cell death, excess Mn^{3+} disproportionates and precipitates as $Mn^{3+/4+}$ oxides on dead fungal residues. These coprecipitates may then accumulate as larger aggregates observed here and elsewhere (24).

Imaging further showed that reactive Mn^{3+} occurs in hotspots at the interface between hyphae and needle epidermis (Fig. 4*C*). These hotspots showed a mixture of Mn^{2+} and reactive Mn^{3+} species and almost no signs of $Mn^{3+/4+}$ oxide accumulation (Fig. 4*A*). If microbially produced Mn^{3+} engages in oxidation reactions with litter components at this interface, it is reduced back to Mn^{2+} in the process. In this scenario, no $Mn^{3+/4+}$ oxides accumulate, and fungi continuously reoxidize Mn^{2+} to form Mn^{3+}. The fact that we find comparable amounts of Mn^{2+} and Mn^{3+} is therefore consistent with active cycling of the $Mn^{2+/3+}$ couple and its involvement in oxidation reactions.

Evidence for chemical alterations of saccharide and aromatic components at infected sites with high Mn^{3+} concentrations reveal a direct involvement of Mn in litter decomposition. First, decreasing absorbance of saccharides in spectra taken from the contact zone between hyphae and epidermis (Fig. 4*E*) is in good agreement with bulk saccharide loss across the litter layers (Table S1) and preferential (hemi)cellulose removal from the site of attack. Second, increased absorbance of bands arising from conjugated C=O and C=C bonds can be attributed to aromatic decomposition products released during the oxidative breakdown of plant material (39, 40). Removal of saccharides and concurrent oxidative alteration of aromatic lignin structures is a widely noted fungal decay pattern, where hyphae generate oxidized trenches in cell walls to liberate and release (hemi) cellulose components without invading the cell interior (41).

In summary, our study reveals the mechanistic link between microbial Mn cycling and the transformations of organic compounds during litter decomposition (Fig. 5*A*). Collectively, our bulk and microscale results show that litter-decomposing fungi first recruit and accumulate reduced Mn^{2+} in the litter layer, transform it into oxidative Mn^{3+} forms at the site of oxidative litter decomposition, and later accumulate it as $Mn^{3+/4+}$ oxide precipitates (Fig. 5*B*). Moreover, we find that Mn oxidation—specifically the formation of reactive Mn^{3+} species—in this ecosystem is not incidental, but tightly coupled to the oxidative degradation of aromatic structures in litter. These findings provide a mechanistic basis for the highly significant "Mn-dependence" (9–11) of litter decomposition across a wide variety of forest ecosystems. Our results suggest that this relationship largely rests on the ability of decomposer organisms to recruit Mn in the litter layer and oxidize it at the site of litter decay. This insight demonstrates that Mn bioavailability and oxidation rate should be recognized as major determinants of litter decomposition in forest ecosystems. Furthermore, it provides strong support for a new ecological concept of litter decomposition: That the ability of decomposer organisms to degrade litter is, in large part, controlled by availability of, and access to, resources critical for the biochemical breakdown of litter.

Our results support the hypothesis that plant–soil systems in forest biomes have coevolved to optimize the "cell-wall degrading machinery" (42), thereby maximizing litter decomposition

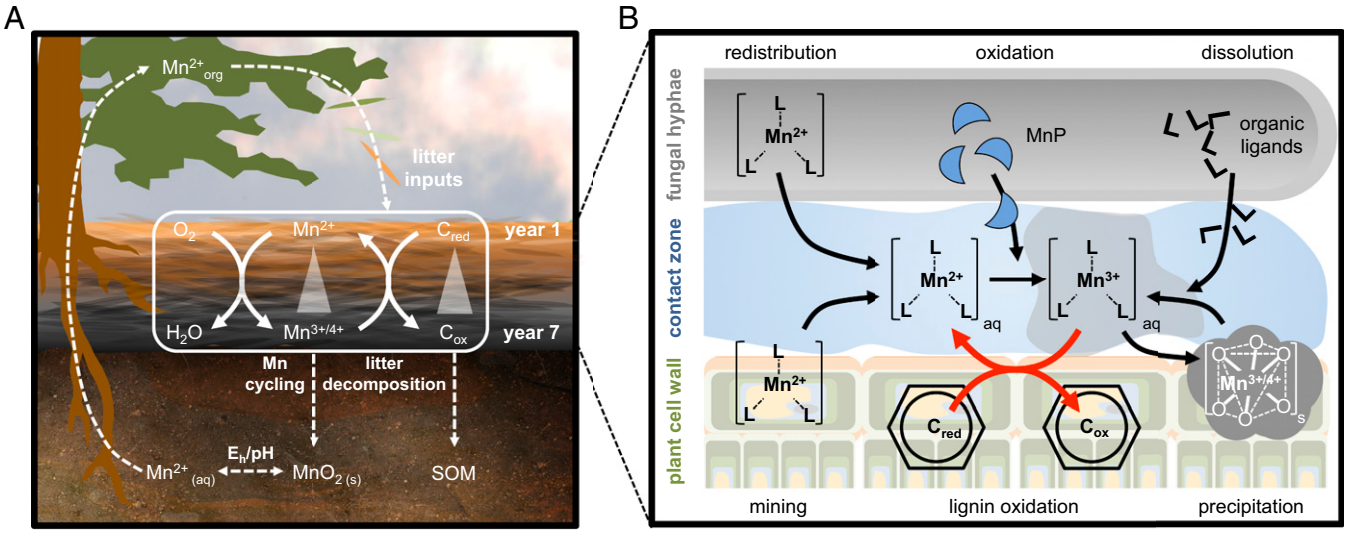

Fig. 5. Macro- and microscale coupling of C and Mn cycles in forest ecosystems. (*A*) Mn cycling through the entire plant–soil system and its link to litter decomposition and SOM formation. (*B*) Microscale Mn cycling by litter-decomposing fungi and its role in the oxidative breakdown of lignin or other aromatic litter components.

(and thus the recycling of nutrients) by ensuring the availability of key resources such as Mn (Fig. 5*A*). Because aspects of global change also impact ecosystem Mn fluxes, bioavailability in soils (43, 44), plant uptake, and foliar litter concentrations (45), the tight coupling we demonstrate between Mn cycling and litter decomposition suggests that further research on regulators of ecosystem Mn fluxes is warranted.

Materials and Methods

Litter Decomposition Study. This study took advantage of an ongoing litter decomposition experiment at the H. J. Andrews Experimental Forest (HJA), Oregon, United States. About 90% of the area's annual precipitation falls from October to April, with the wettest period in December and peak drought conditions occurring in July. Within the HJA, the study was conducted at a site in watershed no. 8, at an elevation of 982 m and slope aspect of 223 degrees. Mean annual temperature at the nearby headquarters averaged 8.8 °C, and annual precipitation was 2,200 mm during 1974–2003 (46). The soil underlying a dense cover of old-growth Douglas fir (*Pseudotsuga menziesii*) is an Andic Dystrudept and shows abundant patches of dense ectomycorrhizal mats (47), which can result in peroxidase activities 28- to 126-times greater than that of nonmat soils (48). We therefore expected particularly rapid Mn cycling at this site.

A "rolling" litter decomposition study spanning the years 2005–2011 was conducted at this site to examine the temporal and spatial variation in litter decomposition across individual layers. Nylon mesh panels (1-mm netting, 60 × 60-cm frames) were placed on the litter surface at this site annually. They were stacked over time to delineate each year's litter fall from the next without confining processes by artificial closure. Upon harvest at the end of the dry season in November 2011, the whole littercake was transferred on a supporting sheet and placed in a sealed plastic container. Fresh needles and underlying O, A, and B horizon material were also collected and transported anaerobically in capped amber vials containing dry ice. Samples were transported at 4 °C and immediately returned to the laboratory. In the laboratory, individual 60 × 60-cm litter layers were separated. Decaying needles were manually isolated from other forms of litter such as cones and twigs, and mixed. Soils were pushed through a 2-mm sieve and mixed thoroughly. Needle litter and soil samples were then stored for further analyses as described in *SI Materials and Methods*.

Manganese Chemistry. Total Mn (as well as Fe, Ca, and Al) content was quantified with X-ray fluorescence spectrometry (XEPOS HE XRF spectrometer; SPECTRO Analytical Instruments). To determine the amount of bioavailable Mn, we additionally conducted Na-pyrophosphate extractions (49), with extractable Mn (Mn_{PYRO}) taken to originate predominantly from soluble and organically complexed Mn (33). Extracted Mn concentrations were measured using inductively coupled plasma mass spectrometry (ICP-MS). Mn oxidation state was determined using Mn XANES (50). Litter and soil samples were dried and hand-ground in an anaerobic glove box and sealed with X-ray transparent Kapton tape. Mn XANES spectra were recorded at the wiggler beamline 4–3 at the Stanford Synchrotron Radiation Lightsource (SSRL) (51).

Litter Decomposition State. Total C and N content was determined using a Europa Scientific 20/20 isotope ratio mass spectrometer. Changes in the organic composition of the decomposing litter were determined using FTIR spectroscopy. FTIR spectra of the samples pressed in KBr pellets were recorded from 4,000 to 650 cm^{-1} with a resolution of 4 cm^{-1} on a Thermo Nicolet NEXUS 670 FTIR spectrometer (Thermo Fisher Scientific).

^{13}C-NMR experiments were performed on a Bruker Avance 400 spectrometer at 100 MHz (400 MHz ^{1}H frequency). All experiments were performed with 4-mm sample rotors in a double-resonance probe head. Semiquantitative structural information on all carbon atoms in the sample was obtained by ^{13}C cross-polarization/total sideband suppression (CP/TOSS). The corresponding subspectrum with signals of nonprotonated carbons and carbons of mobile groups such as rotating CH_3 was obtained by ^{13}C CP/TOSS combined with 40-ms dipolar dephasing (DD).

To identify molecular changes in aromatic components of the litter (lignins and tannins), synchrotron-based laser desorption post ionization (LDPI) mass spectrometry of fresh needles and litter layers was performed on a modified time-of-flight secondary ion mass spectrometer (TOF.SIMS V; IonTOF) coupled to a synchrotron UV light port at beamline 9.0.2 of the Advanced Light Source (ALS) (29, 31). To identify peaks in the resulting mass spectra that corresponded to aromatic structures, ionization energies for each of the most prominent mass peaks were determined as described in ref. 31 and detailed in *SI Materials and Methods*. Based on the low IEs of larger aromatic systems (29, 30), peaks with IEs of less than 8.5 eV were attributed to aromatic moieties.

Chemical Imaging Analyses. Needles from all layers were visibly colonized by fungal hyphae, frequently concentrated around dark infections of the surface. To determine Mn distribution and oxidation state associated with these fungal infections, elemental maps and Mn μXANES spectra of cross-sectioned needle litter were obtained using X-ray fluorescence mapping and absorption spectroscopy (μXRF/XAS) at ALS beamline 10.3.2. To this end, individual needles taken from the top layer were embedded in epoxy (Spurr; TedPella) and cured. Cross-sections were obtained by cutting the resin block and polishing the exposed surface using sand paper and diamond paste.

To obtain high-resolution maps of the functional group chemistry at the hyphae–needle interface, thin sections (<5 μm) of infected needles from the top layer were also prepared using a cryostat (Leica 1950 Cyrostat; Leica Instruments) without the use of carbon-based resins and transferred to gold-coated (IR reflective) microscope slides. High-resolution infrared maps of these locations were acquired using synchrotron FTIR (μFTIR) spectromicroscopy at ALS beamline 1.4.3. After completion of the μFTIR analysis, μXRF maps of the same regions and Mn μXANES spectra of selected points within that region were collected at ALS beamline 10.3.2. Further details on sample preparation, analytical procedures, and data processing can be found in *SI Materials and Methods*.

Data Analysis. All statistical analyses were performed using OriginPro (OriginLab Corp.). Reported SEs are based on three analytical replicates.

ACKNOWLEDGMENTS. We thank J. Sexton for setting up the decomposition study and M. Sarginci for sample processing. We thank M. Marcus and H. Bechtel for help and support at Advanced Light Source beamlines 10.3.2 and 1.4.3, respectively, and E. Nelson for assistance at Stanford Synchrotron Radiation Lightsource beamline 4-3. M. Keiluweit acknowledges funding through a Lawrence Scholar Fellowship awarded by the Lawrence Livermore National Laboratory (LLNL). Funding for M.E.H. and the long-term litter decomposition experiment was provided by a National Science Foundation grant to the H. J. Andrews Long-Term Ecological Research Program (Grant DEB-0823380). Analytical work was performed under the auspices of the US Department of Energy (DOE) by LLNL under Contract DE-AC52-07NA27344. Funding was provided by LLNL Laboratory Directed Research and Development Award 10-ERD-021 "Microbes and Minerals: Imaging C Stabilization" (to J.P.-R., P.N., and M. Kleber), and the work of P.N. was supported by Lawrence Berkeley National Laboratory Award IC006762 as sub-award from LLNL and DOE-Biological and Environmental Research Sustainable Systems scientific focus area. M. Kleber acknowledges support through a research fellowship from the Institute of Soil Landscape Research at the Zentrum für Agrarlandschaftsforschung. Use of the Advanced Light Source is supported by the Director, Office of Science, Office of Basic Energy Sciences, US DOE under Contract DE-AC02-05CH11231. Use of SSRL at the Stanford Linear Accelerator Center National Accelerator Laboratory is supported by the US Department of Energy, Office of Science, Office of Basic Energy Sciences under Contract DE-AC02-76SF00515.

1. Hättenschwiler S, Tiunov AV, Scheu S (2005) Biodiversity and litter decomposition in terrestrial ecosystems. *Annu Rev Ecol Evol Syst* 36(1):191–218.
2. Prescott CE (2010) Litter decomposition: What controls it and how can we alter it to sequester more carbon in forest soils? *Biogeochemistry* 101(1-3):133–149.
3. Chapin FS, Matson PA, Vitousek PM (2011) *Principles of Terrestrial Ecosystem Ecology* (Springer, New York).
4. Cotrufo MF, Wallenstein MD, Boot CM, Denef K, Paul E (2013) The microbial efficiency-matrix stabilization (MEMS) framework integrates plant litter decomposition with soil organic matter stabilization: Do labile plant inputs form stable soil organic matter? *Glob Change Biol* 19(4):988–995.
5. Klotzbücher T, Kaiser K, Guggenberger G, Gatzek C, Kalbitz K (2011) A new conceptual model for the fate of lignin in decomposing plant litter. *Ecology* 92(5):1052–1062.
6. Meentemeyer V (1978) Macroclimate and lignin control of litter decomposition rates. *Ecology* 59(3):465–472.
7. Turner S, Gallois P, Brown D (2007) Tracheary element differentiation. *Annu Rev Plant Biol* 58(1):407–433.
8. Berg B, McClaugherty C (2007) *Plant Litter: Decomposition, Humus Formation, Carbon Sequestration* (Springer, Berlin).
9. Aponte C, García LV, Marañón T (2012) Tree species effect on litter decomposition and nutrient release in mediterranean oak forests changes over time. *Ecosystems (N Y)* 15(7):1204–1218.
10. Berg B, et al. (2010) Factors influencing limit values for pine needle litter decomposition: A synthesis for boreal and temperate pine forest systems. *Biogeochemistry* 100(1-3):57–73.
11. Berg B, Steffen KT, McClaugherty C (2007) Litter decomposition rate is dependent on litter Mn concentrations. *Biogeochemistry* 82(1):29–39.

12. Davey MP, Berg B, Emmett BA, Rowland P (2007) Decomposition of oak leaf litter is related to initial litter Mn concentrations. *Can J Bot* 85(1):16–24.
13. De Marco A, et al. (2012) Decomposition of black locust and black pine leaf litter in two coeval forest stands on Mount Vesuvius and dynamics of organic components assessed through proximate analysis and NMR spectroscopy. *Soil Biol Biochem* 51: 1–15.
14. Heim A, Frey B (2004) Early stage litter decomposition rates for Swiss forests. *Biogeochemistry* 70(3):299–313.
15. Trum F, Titeux H, Cornelis J-T, Delvaux B (2011) Effects of manganese addition on carbon release from forest floor horizons. *Can J For Res* 41(3):643–648.
16. Hofrichter M (2002) Review: Lignin conversion by manganese peroxidase (MnP). *Enzyme Microb Technol* 30(4):454–466.
17. Perez J, Jeffries TW (1992) Roles of manganese and organic acid chelators in regulating lignin degradation and biosynthesis of peroxidases by Phanerochaete chrysosporium. *Appl Environ Microbiol* 58(8):2402–2409.
18. Bugg TDH, Ahmad M, Hardiman EM, Singh R (2011) The emerging role for bacteria in lignin degradation and bio-product formation. *Curr Opin Biotechnol* 22(3):394–400.
19. Diaz JM, et al. (2013) Widespread production of extracellular superoxide by heterotrophic bacteria. *Science* 340(6137):1223–1226.
20. Marschner H (1986) *Mineral Nutrition of Higher Plants* (Academic, Amsterdam).
21. Mukhopadhyay MJ, Sharma A (1991) Manganese in cell metabolism of higher plants. *Bot Rev* 57(2):117–149.
22. Preston CM, Nault JR, Trofymow JA, Smyth C (2009) Chemical changes during 6 years of decomposition of 11 litters in some canadian forest sites. Part 1. Elemental composition, tannins, phenolics, and proximate fractions. *Ecosystems (N Y)* 12(7):1053–1077.
23. Tam S-C, Sposito G, Senesi N (1991) Spectroscopic and chemical evidence of variability across a pine litter layer. *Soil Sci Soc Am J* 55(5):1320–1325.
24. Herndon EM, Martínez CE, Brantley SL (2014) Spectroscopic (XANES/XRF) characterization of contaminant manganese cycling in a temperate watershed. *Biogeochemistry* 121(3):505–517.
25. Blanchette RA (1984) Manganese accumulation in wood decayed by white rot fungi. *Phytopathology* 74(6):725–730.
26. Hansel CM, Zeiner CA, Santelli CM, Webb SM (2012) Mn(II) oxidation by an ascomycete fungus is linked to superoxide production during asexual reproduction. *Proc Natl Acad Sci USA* 109(31):12621–12625.
27. Thompson IA, Huber DM, Guest CA, Schulze DG (2005) Fungal manganese oxidation in a reduced soil. *Environ Microbiol* 7(9):1480–1487.
28. Zhang Y, et al. (2015) Chemical composition of organic matter in a deep soil changed with a positive priming effect due to glucose addition as investigated by 13C NMR spectroscopy. *Soil Biol Biochem* 85:137–144.
29. Hanley L, Zimmermann R (2009) Light and molecular ions: The emergence of vacuum UV single-photon ionization in MS. *Anal Chem* 81(11):4174–4182.
30. Adam T, Zimmermann R (2007) Determination of single photon ionization cross sections for quantitative analysis of complex organic mixtures. *Anal Bioanal Chem* 389(6):1941–1951.
31. Liu SY, et al. (2013) Synchrotron-based mass spectrometry to investigate the molecular properties of mineral-organic associations. *Anal Chem* 85(12):6100–6106.
32. Takahashi LK, et al. (2011) Vacuum-ultraviolet photoionization and mass spectrometric characterization of lignin monomers coniferyl and sinapyl alcohols. *J Phys Chem A* 115(15):3279–3290.
33. Sposito G (2008) *The Chemistry of Soils* (Oxford Univ Press, Oxford), 2nd Ed.
34. Preston CM, Nault JR, Trofymow JA (2009) Chemical changes during 6 years of decomposition of 11 litters in some canadian forest sites. Part 2. 13C abundance, solid-state 13C NMR spectroscopy and the meaning of "lignin." *Ecosystems (N Y)* 12(7): 1078–1102.
35. Šnajdr J, et al. (2011) Transformation of Quercus petraea litter: Successive changes in litter chemistry are reflected in differential enzyme activity and changes in the microbial community composition. *FEMS Microbiol Ecol* 75(2):291–303.
36. Ponge J-F (1988) Étude écologique d'un humus forestier par l'observation d'un petit volume. III. La couche F1 d'un moder sous Pinus sylvestris. *Pedobiologia (Jena)* 31(1-2): 1–64.
37. Ponge J-F (1985) Étude écologique d'un humus forestier par l'observation d'un petit volume. II. La couche L2 d'un moder sous Pinus sylvestris. *Pedobiologia (Jena)* 28(2): 73–114.
38. Ponge J-F (1984) Étude écologique d'un humus forestier par l'observation d'un petit volume, premiers résultats. I. La couche L1 d'un moder sous pin sylvestre. *Revue d'Ecologie et de Biologie du Sol* 21(2):161–187.
39. Stewart D (1996) Fourier transform infrared microspectroscopy of plant tissues. *Appl Spectrosc* 50(3):357–365.
40. Yu H, Hu J, Fan J, Chang J (2012) One-pot conversion of sugars and lignin in ionic liquid and recycling of ionic liquid. *Ind Eng Chem Res* 51(8):3452–3457.
41. Martínez AT, et al. (2005) Biodegradation of lignocellulosics: Microbial, chemical, and enzymatic aspects of the fungal attack of lignin. *Int Microbiol* 8(3):195–204.
42. Eastwood DC, et al. (2011) The plant cell wall-decomposing machinery underlies the functional diversity of forest fungi. *Science* 333(6043):762–765.
43. Cheng L, et al. (2010) Atmospheric CO_2 enrichment facilitates cation release from soil. *Ecol Lett* 13(3):284–291.
44. Natali SM, Sañudo-Wilhelmy SA, Lerdau MT (2009) Plant and soil mediation of elevated CO_2 impacts on trace metals. *Ecosystems (N Y)* 12(5):715–727.
45. Lynch JP, St.Clair SB (2004) Mineral stress: The missing link in understanding how global climate change will affect plants in real world soils. *Field Crops Res* 90(1): 101–115.
46. Sulzman EW, Brant JB, Bowden RD, Lajtha K (2005) Contribution of aboveground litter, belowground litter, and rhizosphere respiration to total soil CO2 efflux in an old growth coniferous forest. *Biogeochemistry* 73(1):231–256.
47. Griffiths RP, Caldwell BA, Cromack K, Jr, Morita RY (1990) Douglas-fir forest soils colonized by ectomycorrhizal mats. I. Seasonal variation in nitrogen chemistry and nitrogen cycle transformation rates. *Can J Res* 20(2):211–218.
48. Griffiths RP, Caldwell BA (1992) Mycorrhizal mat communities in forest soils. *Mycorrhizas in Ecosystems*, eds Read DJ, Lewis DH, Fitter AH, Alexander I (CAB International, Wallingford, UK).
49. Courchesne F, Turmel MC (2007) Extractable Al, Fe, Mn, and Si. *Soil Sampling and Methods of Analysis*, eds Carter MR, Gregorich EG (CRC, Boca Raton, FL), 2nd Ed.
50. Manceau A, Marcus MA, Grangeon S (2012) Determination of Mn valence states in mixed-valent manganates by XANES spectroscopy. *Am Mineral* 97(5-6):816–827.
51. Lytle FW, et al. (1984) Measurement of soft X-ray absorption spectra with a fluorescent ion chamber detector. *Nucl Instrum Methods Phys Res A* 226(2–3):542–548.
52. Ravel B, Newville M (2005) ATHENA, ARTEMIS, HEPHAESTUS: Data analysis for X-ray absorption spectroscopy using IFEFFIT. *J Synchrotron Radiat* 12(Pt 4):537–541.
53. Mao J-D, et al. (2000) Quantitative characterization of humic substances by solid-state carbon-13 nuclear magnetic resonance. *Soil Sci Soc Am J* 64(3):873–884.
54. Skjemstad J, Frost R, Barron P (1983) Structural units in humic acids from south-eastern Queensland soils as determined by 13nmr spectroscopy. *Soil Res* 21(4):539–547.
55. Solomon D, et al. (2007) Long-term impacts of anthropogenic perturbations on dynamics and speciation of organic carbon in tropical forest and subtropical grassland ecosystems. *Glob Change Biol* 13(2):511–530.
56. Kögel-Knabner I (2002) The macromolecular organic composition of plant and microbial residues as inputs to soil organic matter. *Soil Biol Biochem* 34(2):139–162.